Design of Magnetoplasmonic Resonant Nanoantennas for Biosensing Applications

M. Essone Mezeme and C. Brosseau*
Lab-STICC, Université Européenne de Bretagne, Université de Bretagne Occidentale
*Corresponding author: CS 93837, 6 avenue Le Gorgeu, 29238 Brest Cedex 3, France, brosseau@univ-brest.fr

Abstract: We present a numerical model we have created and verified to characterize the frequency dependence of the effective magnetic permeability and permittivity of a core-shell (CS) nanostructure composed of a magnetic core and a plasmonic shell with well-controlled dimensions for different geometries and polarizations. We analyze several possible shell shapes involving sharp edges and tips. The model sets the foundation of quantitatively determining the spatial confinement of the electric field in regions ≈ 20 nm in linear dimension. The practical rational for this research direction is the importance of the microwave functionality of the magnetic (core) nanoparticle and the optical properties of the plasmonic shell for characterizing biological cells. The ability to manipulate and remotely control specific cellular components by optical antennas has the potential to provide scientists and clinicians a powerful tool for investigating cell function and molecular signalling pathways, as well as to provide a platform for the development of new treatments.

Keywords: nanoantenna, magnetoplasmonics, core-shell nanostructure, finite element simulation

1. Introduction

In this paper, we investigate the long-wavelength electromagnetic properties of resonant magnetoplasmonic CS nanostructures with well-controlled dimensions. Although the role of the PLRs and interface phenomena in such CS nanostructure extends beyond any specific example, the present study has been motivated by our interest in nanoantenna based on hybrid magnetoplasmonic $C(Fe_3O_4)S(Au)$ nanostructures for biological applications, i.e. the dielectric properties of the host matrix can be assimilated to water. In our investigation we have carried out FE calculations on a 2D (3D infinitely long cylinder) model [1-5]. Ideally, one would like to study a CS nanostructure in the form of a 3D finite structure. However, we adopt here the same notations and conventions as in [1] because computations in 2D are more tractable than in 3D. Importantly, our results show a significant sensitivity of the shape anisotropy of the CS to its electromagnetic parameters. As will be discussed in detail below, these results are complimentary to those obtained on isotropic CS nanostructures as discussed in the recent literature [1-6]. To illustrate the effects of shape anisotropy of the structure, we analyze several possible CS nanostructures shell shapes involving sharp edges and tips. This permits to investigate the effects of geometric parameters for a given CS nanostructure and exciting field polarization on the PLR spectral position. Finally, we also examine the effects of these parameters on the intensity of the electric field enhancement (EFE) and magnetic field enhancement (MFE). We show that the effective active area, corresponding to the largest values of the EFE (hot spots), is a small fraction of that occupied by the CS nanostructure. We present data which strongly indicate that the PLR is locally amplifying the electric field in regions $\approx$20 nm in linear dimension.

2. Preliminaries

2.1 Model of the CS nanoantenna

As in many earlier calculations of the effective electromagnetic properties of heterostructures, the essential ingredients in the simple model we consider are as follows. (i) An important simplification takes place if one is interested only in the long-wavelength behavior of the system. The validity of this mean-field approximation is rooted in the fact that all length scales must be much smaller than the wavelength of radiation, or equivalently that the effective wavelength for the composite should be larger than ξ, where ξ denotes a typical length scale that characterizes the inhomogeneities in the material medium. Put in this way, this crucial constraint provides an upper bound to F, i.e. F

$\leq c\sqrt{\Phi/(\pi R^2 \varepsilon' \mu')}$, where Φ denotes the surface fraction of the CS inclusion [7]. (ii) We use a continuum modelling approach built upon constitutive equations which can capture the material behavior on experimentally relevant scales, i.e. the local electrical response in terms of a position dependent permittivity. (iii) We further assume that within these linear response calculations, only linear effects are accessible to this technique, i.e. the interaction of the CS structure with the electromagnetic wave is modelled by induced electric and magnetic dipole moments. Notice that the penetration depth of electromagnetic waves at optical frequencies is about 20 nm for Au.

Fig. 1 illustrates the simple yet sufficiently realistic geometry we are interested in. Specifically, we consider a cross-sectional view of a CS nanostructure composed of a magnetic core (black area, phase 3) which is coated by a plasmonic shell (grey area, phase 2).

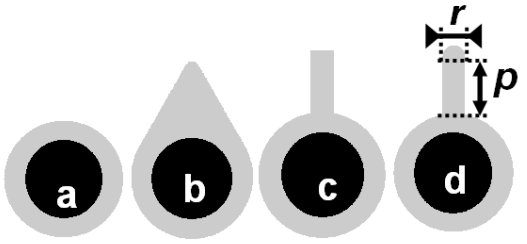

Figure 1: Illustrative examples of CS nanostructures considered: (a) isotropic case; (b), (c), and (d) refer to representative anisotropic CS nanostructures situations where the shell of the CS nanostructures involves sharp edges and tips.

The parameterization involved in the modelling is schematically described in Fig. 2. In our simulations, *R*-*e*=30 or 45 nm, the surface fraction of the Au phase is fixed to 0.033 and Φ was kept constant to 0.1, i.e. we restrict to the dilute limit corresponding to dipolar properties. Frequency-space descriptions, in which the fields have a harmonic time evolution $\propto \exp(-j2\pi Ft)$, allow describing the complex permittivity and magnetic permeability of the phases by $\varepsilon_i(F) = \varepsilon'_i - j\varepsilon''_i$ and $\mu_i(F) = \mu'_i - j\mu''_i$, respectively; where the index *i* denotes the phase. The CS nanostructure is embedded in a host medium (phase 1). The choice of value for the intrinsic permittivity of phase 1 is specific to the application we have in mind, i.e. to create new functional materials for applications in a biological environment.

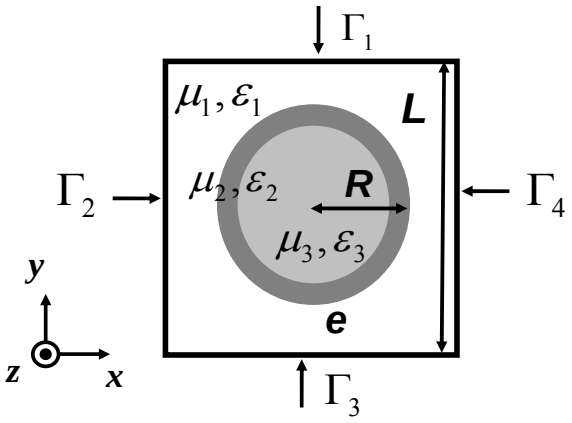

Figure 2: Cross-sectional view for the infinite CS nanostructure (i.e. for type a) investigated. The square cell has size *L* in the *x*-*y* direction and is infinitely extended in the *z* direction. Since typical values of the radius and shell thickness are *R*=50 nm and *e*=5 nm, respectively, the shell thickness is greatly exaggerated in this figure.

The next simplification of the model we make in order to provide a simple physical picture is to consider that phase 3 is uniformly and totally magnetized (macro spin). For the purposes of this paper we adopt the following set of definitions: $\mu_1 = \mu_2 = 1$, and the spectral function for μ_3 we shall focus on is $\mu_3(F) = 1 + F_M(F_0 + j\alpha F)/((F_0 + j\alpha F)^2 + F^2)$ $= \mu'_3 - j\mu''_3$, with $F_M = \gamma M_S / 2\pi$, $F_0 = \gamma H_0 / 2\pi$, and $F_R = F_0/\sqrt{1+\alpha^2}$. In the case considered here, the magnetic permeability can be obtained from the Landau-Lifshitz-Gilbert equation [8], which describes the precession motion of the magnetization in an effective magnetic field. As usual, M_s denotes the saturation magnetization, γ is the gyromagnetic ratio of the electron, H_0 is the resonant magnetic field, and α is the Gilbert damping parameter. In our analysis we have used the values $\gamma/2\pi$=2.8 GHz/kOe, M_S = 70 Oe, F_R = 4.5 GHz, and $\alpha=10^{-2}$ reported for pure Fe_3O_4 [8]. Table 1 summarizes the actual numerical values of the parameters used in this paper.

Parameter	Au	Fe_3O_4
$\varepsilon_\infty^{'}$	7	4.73
F_p (Hz)	2.23 10^{15}	7.25 10^{12}
τ (s)	2.65 10^{-14}	8 10^{-14}

Table 1. Main dielectric parameters used in this analysis.

It is common practice to express the intrinsic (relative) permittivity of the surrounding media (as previously mentioned, the dielectric properties of the host matrix can be assimilated to water) in the form $\varepsilon_1(F) = \varepsilon_1^{'} - j/(2\pi F \varepsilon_0)$, where $\varepsilon_1^{'} = 80$ (resp. $\varepsilon_1^{'} = 1.77$) in the GHz (resp. THz) range of frequencies [9]. Following Drude, the intrinsic (relative) permittivity can be written as $\varepsilon\ (F) = \varepsilon'_\infty - F_p{}^2/(F^2 - jF(2\pi\tau)^{-1})$. These generic parameter values are only illustrative and have been chosen since they can be helpful for biomedical applications.

2.2 Numerical simulation

We briefly examine the principle of our numerical method viewed from the continuum perspective. Our theoretical studies are performed using finite element (FE) calculations implemented within the FE Comsol Multiphysics simulation package. We treat the calculations of the effective magnetic permeability and permittivity simultaneously. The details and implications of the FE meshing method were discussed in Refs. [1-3,10]. Although involved in some of its details, our procedure is conceptually simple. Unless otherwise specified, ε and μ were calculated by considering as a model system a square cell of size L (Fig. 2) with periodic boundary conditions by imposing V=V_2=1 V on Γ_1, V=V_1=0 V on Γ_3 and $\partial V/\partial n = 0$ on Γ_2 and Γ_4, and J=J_2=1 Am^{-2} on Γ_1, J=J_1=-1 Am^{-2} on Γ_3 et $\boldsymbol{H}\times\boldsymbol{n} = \boldsymbol{0}$ on Γ_2 and Γ_4.

A few comments are in order. In order to validate this method and characterize the generality of the behavior we observe, a first indicator is to compare these values with those evaluated by Wiener and Hashin-Shtrikman bounds. Skipping the details, we just announce the conclusion: for a wide range of parameters, our numerical results compare favorably with theoretical predictions by Wiener and HS bounds of the region of the complex plane inside which values of ε and μ are allowed. As a further cross-check of method and a practical test of the quality of the numerical calculations for the electromagnetic parameters, the calculated effective ε and μ were also compared to independent predictions given by the Kramers-Kronig (KK) relations which, as described in e.g. [10], require no assumptions about the nature of the polarization or magnetization behaviors. The residual errors in, e.g. $\varepsilon^{'}$, with respect to the value obtained from KK relation were less than 0.5 % throughout the entire frequency range investigated.

3. Results and discussion

We begin by showing in Fig. 3 some plots of the real and imaginary parts of the effective magnetic permeability spectra (4 GHz<F<5 GHz) for R-e=30 nm.

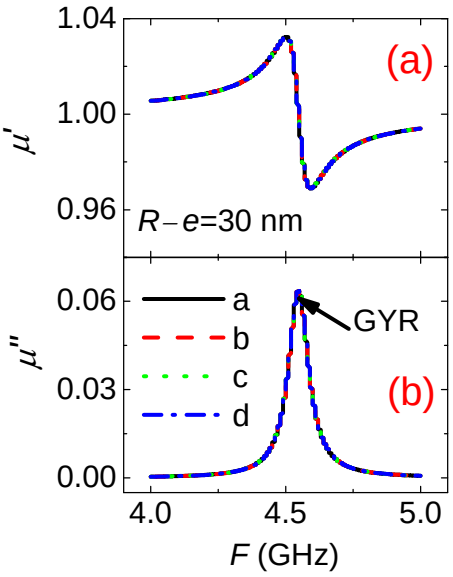

Figure 3. (a) The real part of the complex effective magnetic permeability is plotted versus frequency of the magnetic field, for the CS structures considered in Fig. 1 and R-e=30 nm. The letters and corresponding lines (black: a, red: b, green: c, and blue: d) refer to the structures displayed in Fig. 1. The magnetic field is defined to be along the x-axis. (b) Same as in (a) for the imaginary part of the complex effective magnetic permeability.

Fig. 3 (a)-(b) reveal two remarkable features. First, we note the unambiguous evidence of the gyromagnetic resonance (GYR) at a spectral position close to that of pure Fe_3O_4 (4.5 GHz) as expected. The second feature of these figures is that the curves for the four examples of CS nanostructures are exactly overlaid over the entire range of frequency explored, suggesting that the effective demagnetizing field is similar in each case. In addition, the values of μ do not depend (not shown) on the direction of the magnetic field taken to calculate μ as expected. Fig. 4 depicts the simulation of the spatial distribution of the MFE for the gyresonance mode (4.53 GHz) for the four CS structures considered in Fig. 1. The maximum value attained by the MFE is directed along the x axis, is localized in the core of the nanostructure, and is ≈ 1.5.

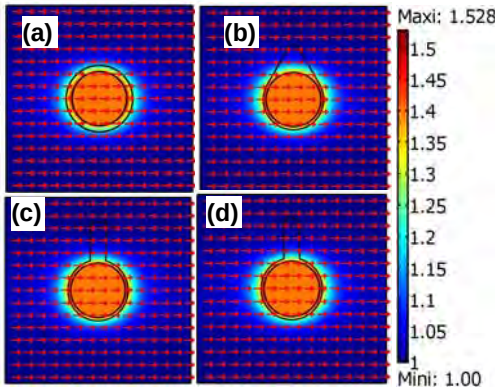

Figure 4. Spatial distribution of the magnetic field enhancement (MFE) for the gyresonance mode (4.53 GHz) for the 2D CS structure considered in the inset of FIG. 1. $\Phi = 0.1$, R=50 nm and e=5 nm. The arrows indicate the orientation of the magnetic field.

Having discussed the general trend of μ as a function of frequency in the GHz range and its relation to the geometry of the CS nanostructure some comments have to be made yet about the spectral evolution of ε in the few hundreds of THz range. The results of this analysis are shown in Fig. 6 R-e=30 nm. Figs. 5 (a) and (b) illustrate how the real and imaginary parts of the effective permittivity spectra (100 THz<F<500 THz) vary when the electric field is along the x-axis or the y-axis for the four CS nanostructures. The tunability of the PLR as a function of the orientation of the applied electric field and the shape of the structure can be clearly seen. The most striking feature of these graphs is the blueshift (resp. redshift) of the PLR when passing from the isotropic shape of structure a to the anisotropic shapes of structures b, c, and d.

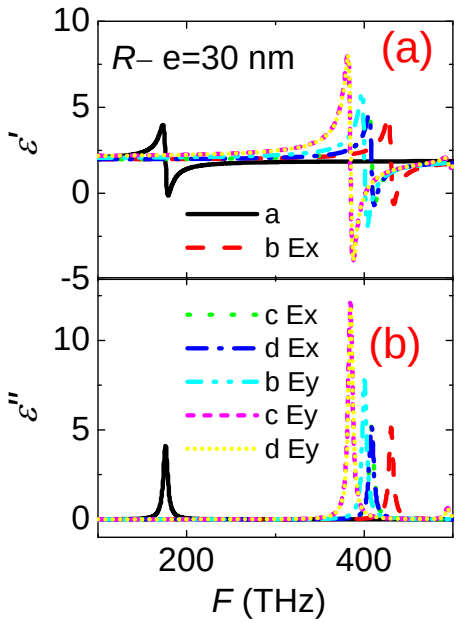

Figure 5. (a) Evolution of the spectral behavior of the real part of the effective permittivity for the CS structures considered in Fig. 1 and R-e=30 nm. The letters and corresponding lines (black: a, red: b, green: c, dark blue: d, light blue: b, pink: c, and yellow: d) refer to the structures displayed in Fig. 1. The electric field is defined to be either along the x-axis (Ex) or the y-axis (Ey). (b) Same as in (a) for the imaginary part of the effective permittivity of the complex effective permittivity.

We also discuss the sensitivity of the maximum value of the EFE as a function of frequency of the electric field. Fig. 6 (a) shows the EFE data for the structure a at PLR for the selected value R-e=45 nm. For comparison, the local EFE map plotted in the middle and bottom panels of Fig. 6 provide electrical field information of the structure d for the two polarizations of the electric field. A notable feature of Fig. 6 is that the maximum EFE is a factor of two larger when the electric field is

oriented along the *y*-axis than when the field is polarized along the *x*-axis.

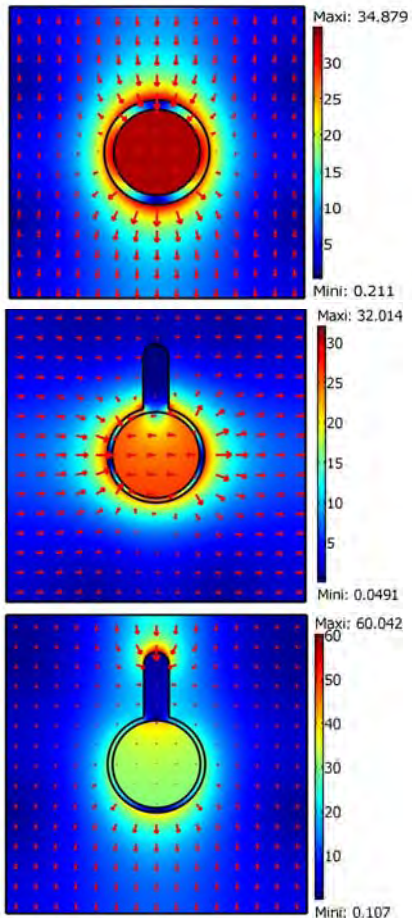

Figure 6. (top) Visualization of the EFE for CS structure a and PLR=346 THz corresponding to *R*-*e*=45nm. The electric field is oriented along the *y*-axis. (middle) Same as in top for CS structure d and *F*=271 THz. The electric field is oriented along the *x*-axis. (bottom) Same as in middle for *F*=247 THz. The electric field is oriented along the *y*-axis.

While the simulations so far have been for the four examples of CS nanostructures shown in Fig. 1, we now move on to consider the structure d in more detail. For that purpose, we consider two geometric parameters, denoted by *r* and *p*, whose significance is shown in Fig. 1. This is illustrated in Fig. 7 which presents the spectral characteristics of the impedance for a selected set of numerical values of the parameters listed in Table 2.

Parameter	d	d_1	d_2	d_3	d_4
R-*e* (nm)	45	45	45	45	45
e (nm)	5	7	5	3	5
r (nm)	26	18	18	34	34
p (nm)	54	54	88	54	37
r/*r*(*d*)	1.0	0.7	0.7	1.3	1.3

Table 2. Values of *r* and *p* considered for the calculations leading to Figs. 7-8 (see Fig. 1 for their respective definition)

Fig. 7 shows the relation between the geometric parameters *r* and *p* and the magnitude of the effective permittivity both in real and imaginary parts.

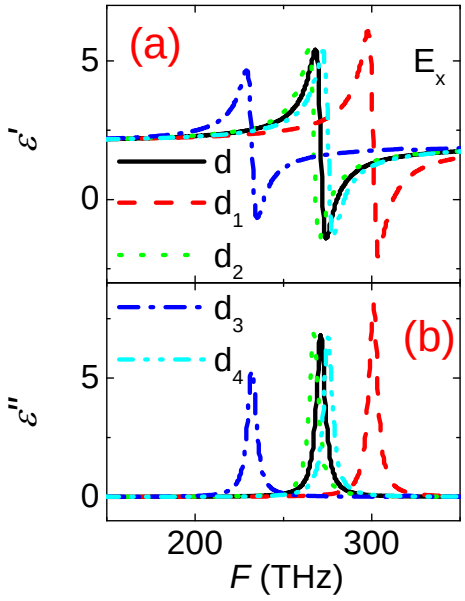

Figure 7. (a) Evolution of the spectral behavior of the real part of the effective permittivity for several variants of the d CS structure displayed in Fig. 1 and *R*-*e*=45 nm. The letters and corresponding lines (black: d, red: d_1, green: d_2, dark blue: d_3, light blue: d_4) refer to the d structure with values of *r* and *p* listed in Table 2. The electric field is directed along the *x*-axis (Ex). (b) Same as in (a) for the imaginary part of the effective permittivity of the complex effective permittivity. (c) Same as in (a) for the modulus of the impedance. (d) Same as in (c) for the phase of the impedance.

The next point to be discussed is the large magnitude of the EFE (Fig. 8).

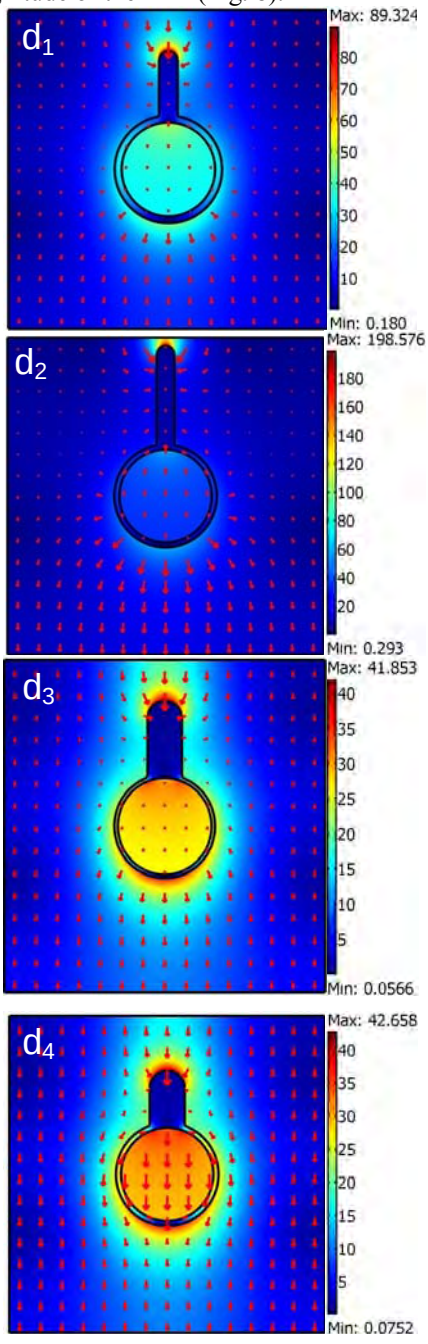

Figure 8. (top) Visualization of the EFE for CS structure d_1 and PLR=300.7 THz corresponding to *R-e*=45nm. (d_2) Same as in top for CS structure d_2 and *F*=267.1 THz. (d_3) Same as in top for structure d_3 and *F*=232 THz. (d_4) Same as in top for structure d_4 and 275.2THz The electric field is oriented along the *x*-axis.

Based on the observed EFE increase of ≈ 5.8 for the parallel versus perpendicular (to the CS nanoparticle axis) excitation polarization, it is possible to make an estimate of the spatial confinement of the optical energy in regions ≈ 20 nm in linear dimension. Interestingly, in Fig. 8, we show the contrasting behavior of the magnitude of the EFE for a given electric field polarization and varying geometric parameters. Our finding points to the important fact that by adjusting the ratio $r/r(d)$, the PLR can be tailored at other frequency range for a given CS structure. Comparing the values of $r/r(d)$ in Table 2, which were chosen to be less (d_1 and d_2) or higher (d_3 and d_4) than 1, we find that the maximum value of the EFE is larger in the former case.

Based on the preceding results, one expects that this computational electromagnetic design approach for the spectral response of polarization-sensitive optical nanoantennas with respect to their geometric and modelling parameters may have interesting implications in both science and technology. However, in order for this potential to be realized in a practical manner, we need to better understand the precise role of materials and structures which can be chosen to enable the transmitter-receive pair concept to be effective without unwanted antenna coupling or cross-talk. This presents the possibility of a trade-off between PLR bandwidth and quality factor which is important in the context of plasmon sensor applications. Calculations of such effects are cumbersome and thus beyond the scope of this present work. Second, largely for reasons of calculational convenience, in the present paper, we focused only on 2D simulations. The methodology can be trivially extended to 3D configurations. Of course, if the goal is to control the EFE due to the plasmonic resonance, forms other than those considered here are possible. There is further room for optimization of the shape and size of the CS nanostructure, e.g. nanowires, nanostar.[29] Third, we end with a discussion of the broader implications of our findings in light of recent experiments. There are very recent sets of experiments which suggest that composite nanoparticle systems with controlled magnetic and plasmonic properties have great potentials in tissue imaging, drug delivery, and information storage. Using the finite-difference time-domain method, Hao *et al.* [11] showed that the plasmonic properties of a nanostar result from

hybridization of plasmons of the core and tips of the nanoparticle. The nanostar core serves as a nanoscale antenna, dramatically increasing the excitation cross section and the electromagnetic field enhancements of the tip plasmons. Other authors found that the permittivity of the core material, not the shape of the core, is a major controlling factor in the PLR of CS nanoparticles [12]. On the basis of our investigation, we further conclude-in accordance with Ref. [12]- that the specific concentration of the metallic phase must be considered as another important quantity for the tunability of the plasmonic properties of CS nanoparticles. A model system that has received particular recent attention is the combination of ferromagnetic and plasmonic nanomaterials whose properties allow developing new strategies for simultaneous cancer therapy and diagnostics. Recent advances in active plasmonic devices, i.e. for which the magnetic field can modulate the plasmon properties, also offer new opportunities for the design of plasmon-based telecommunications applications.

4. Summary

To summarize, we have conducted linear response calculations of the long-wavelength electromagnetic properties of resonant magnetoplasmonic nanostructures composed of CS nanoparticles with well-controlled dimensions. Using the model and the method presented here, the sensitivity of the simulated results have been analyzed for several key effects, namely, (i) the influence of geometric parameters characterizing the shape of the CS nanostructures and the orientation of the exciting electric field. We have shown that the physical properties of the CS nanostructures can be tuned by properly selecting dielectric and magnetic components with specific intrinsic material parameters. Resonant gyromagnetic and plasmonic effects result in significant MFE and EFE. We found nanolocalized THz fields corresponding to large EFE two orders of magnitude higher in amplitude than the excitation optical field. Further, by repeating similar numerical experiments for various anisotropic CS configurations, we found that these CS structures possess a broadband and polarization sensitive PLR which can be highly dependent on the shape of the nanostructure. Another outcome of the present study is that these CS structures are characterized by nanoscale field distributions. The latter property is important because they allow for manipulation at the nanoscale dimensions, i.e. they confine and guide optical energy over distances much smaller than the wavelength. This behavior is most prevalent for the structure d displayed in Fig. 1. (ii) A significant part of our focus in this paper was on a careful analysis of the effective characteristic impedance of these wave-guide based nanostructures that is playing a key role in the study of propagation losses. Although these results were obtained only for a very specific model (2D nanostructures corresponding to infinite cylinders in 3D), these proved to be useful in understanding the spectral response of nanoantennas.

5. References

1. M. Essone Mezeme, S. Lasquellec, and C. Brosseau, Phys. Rev. E **81**, 057602 (2010).
2. M. Essone Mezeme and C. Brosseau, J. Appl. Phys. **107**, 014701 (2010).
3. M. Essone Mezeme and C. Brosseau, J. Appl. Phys. **108**, 014701 (2010).
4. D. R. Fredkin, and I. D. Mayergoyz, Phys. Rev. Lett. **91**, 253902 (2003).
5. R. C. McPhedran, L. Poladian, and G. W. Milton, Proc. R. Soc. Lond. A **415**, 185 (1988); L. Poladian, Q. J. Mech. Appl. Math. **41**, 395 (1988); L. Poladian, Ann. Phys. **188**, 386 (1988).
6. E. Prodan and P. Nordlander, J. Chem. Phys. **120**, 5444 (2004); E. Prodan, C. Radloff, N. J. Halas, P. Nordlander, Science **302**, 419 (2003).
7. C. Fourn, S. Lasquellec, and C. Brosseau, J. Appl. Phys. **102**, 124107 (2007); C. Fourn and C. Brosseau, Phys. Rev. E **77** 016603 (2008); P. Salou, A. Mejdoubi, and C. Brosseau, J. Appl. Phys. **105**, 114702 (2009).
8. J. Ben Youssef and C. Brosseau, Phys. Rev. B **74**, 214413 (2006).
9. E. D. Palik, *Handbook of Optical Constants of Solids* (Academic, San Diego, 1998).
10. M. Essone Mezeme, S. Lasquellec, and C. Brosseau, J. Phys. D **42**, 135420 (2009).
11. F. Hao, C. L. Nehl, J. H. Hafner, and P. Nordlander, Nano Lett. **7**, 729 (2007).
12. R. Bardhan, W. Chen, C. Perez-Torres, M. Bartels, R. M. Huschka, L. L. Zhao, E. Morosan, R. G. Pautler, A. Joshi, and N. Halas, Adv. Funct. Mater. **19**, 3901 (2009).